Stable Liquid Sulfur Generation on Transition Metal Dichalcogenides Toward Low-Temperature Lithium-Sulfur Batteries

Fangyi Shi,[1] Nicolas Onofrio,[2] Chunhong Chen,[3] Songhua Cai,[1] Yanyong Li,[1] Lingling Zhai,[1] Lyuchao Zhuang,[1] Zheng-Long Xu[3,4,5]*, Shu Ping Lau[1]*

1. Department of Applied Physics, Research Institute for Smart Energy, The Hong Kong Polytechnic University, Hung Hom, Hong Kong, P.R. China.
2. Institut Européen des Membranes, IEM, UMR 5635, Univeristé Montpellier, ENSCM, CNRS, Montpellier 34000, France.
3. Department of Industrial and Systems Engineering, The Hong Kong Polytechnic University, Hung Hom, Hong Kong, P.R. China.
4. State Key Laboratory of Ultraprecision Machining Technology, The Hong Kong Polytechnic University, Hung Hom, Hong Kong, P.R. China.
5. Hong Kong Polytechnic University Shenzhen Research Institute, Shenzhen, 518057, PR China

Correspondence authors. Email: apsplau@polyu.edu.hk (S.P.L.) and Email: zhenglong.xu@polyu.edu.hk (Z.L.X.)

ABSTRACT

The electrochemical formation of liquid sulfur at room temperature on the basal plane of MoS_2 has attracted much attention due to the high areal capacity and rapid kinetics of lithium-liquid-sulfur chemistry. However, the liquid sulfur is converted to the solid phase once contacting the solid sulfur crystals generated from the edge of MoS_2. Thus, stable liquid sulfur cannot be formed on the entire MoS_2 surface. Herein, we report entire liquid sulfur generation on hydrogen-annealed MoS_2 (H_2-MoS_2), even under harsh conditions of large overpotentials and low working temperatures. The origins of the solely liquid sulfur formation are revealed as the weakened interactions between H_2-MoS_2 and sulfur molecules and the decreased electrical polarization on the edges of the H_2-MoS_2. The progressive nucleation and droplet-merging growth behaviors are observed during the sulfur formation on H_2-MoS_2, signifying high areal capacities by releasing active H_2-MoS_2 surfaces. To demonstrate the universality of this strategy, other transition metal dichalcogenides (TMDs) annealed in hydrogen also exhibit similar sulfur growing behaviors. Furthermore, H_2 annealing treatment can induce sulfur vacancies on the basal plane and partial oxidation on the edge of TMDs, which facilitates liquid sulfur formation. Finally, the liquid sulfur can generate on H_2-MoS_2 flakes at an ultra-low temperature of -50 °C, which provides possible development for low-temperature lithium-sulfur batteries. This work demonstrates the potential of the pure liquid sulfur-lithium electrochemical system using functionalized two-dimensional materials.

Keywords: liquid sulfur, MoS_2, lithium-sulfur battery, *in-situ* optical microscopy, low-temperature battery

Lithium-sulfur batteries (LSBs) with high theoretical energy densities of 2600 Wh kg^{-1} and low cost of sulfur feedstock have been considered promising alternatives to the commercial lithium-ion batteries to meet increased energy demanding applications such as electric vehicles. [1, 2] However, the practical implementation of LSBs has been hindered by several fundamental challenges associated with the complex Li-S conversion reactions, including the insulating nature of active materials, the shuttle effect, sluggish conversion kinetics of polysulfide intermediates (Li_2S_n, $4 \leq n \leq 8$), and the large volume expansion (80%) of sulfur during lithiation. [3, 4] Tremendous efforts have been devoted to engineering the chemistry and structures of sulfur-containing hosts, [5, 6] promoting the entrapment and conversion of polysulfides,[7, 8] and examining the structural evolutions of sulfur species during cycling. [9, 10] The soluble polysulfides in electrolyte and complex discharging processes (S_8 (solid) $\rightarrow Li_2S_n$ ($4 \leq n \leq 8$, liquid) $\rightarrow Li_2S$ (solid)) have been studied in detail, but relatively little is known about the charging process and products (S_8).

Studies by X-ray diffraction (XRD),[11, 12] transmission electron microscopy (TEM)[13, 14] and X-ray absorption spectroscopy (XAS)[15] indicate that the Li_2S crystal is oxidized to soluble polysulfides and further to solid sulfur in β phase during the charging process. However, some researchers recently found an unusual phenomenon under operando optical microscopy: the charging product (S_8) would be in the liquid phase instead of being solid in an electrochemical cell at room temperature.[16] The sulfur droplets obtained through electrochemical reaction far below their melting temperature (155 °C) well enable the development of high-energy liquid LSBs, electroactive flow devices, and liquid microlensing applications.[17] Simultaneously observing the sulfur growth and electrochemical behaviors found that liquid sulfur droplets can induce higher areal capacities than solid sulfur crystals under the same operating conditions due to releasing active sites/substrates by coalescence of sulfur droplets. [18] In addition, the fast dynamic and

supercooled nature of the sulfur droplets signify possibly fast-charging and low-temperature liquid S-Li batteries.

Nevertheless, Yang *et al.*[18] found that the liquid sulfur generated on the basal plane of two-dimensional (2D) layered materials (*i.e.*, MoS_2) would be solidified by touching solid sulfur crystals, which would grow and propagate from the edge upon charging. As a result, the complete coverage of insulating solid sulfur on MoS_2 stalled the electrochemical reaction. Instead, the strong electric field polarization dominantly caused the edge-induced crystallization on the edge areas of MoS_2 flakes. To eliminate the edge effect, they either conformally covered the MoS_2 edges with titanium/SiO_2 layers or deposited MoS_2 monolayers, which are considerably expensive, elaborative, and infeasible for practical applications. Thus, a significant challenge is to develop efficient strategies or materials to sustain the appealing liquid sulfur for high-performance liquid sulfur-based energy storage technology.

This contribution demonstrates only liquid sulfur generation from delithiation of polysulfides on MoS_2 flakes annealed in an H_2 ambient (designated as H_2-MoS_2). Both optical and Raman spectroscopy observations reveal that the liquid sulfur phase sustains on the basal plane of H_2-MoS_2 without solid sulfur growing from the edge area, even charging the electrochemical system up to 3.5 V *vs.* Li/Li^+. Combined experimental and theoretical investigations elucidate the mechanism of eliminating edge-induced sulfur crystallization. We find that the binding energies between sulfur molecules and H_2-MoS_2 are lower than those for pristine MoS_2, which weakens the local sulfur supersaturation and wettability on the edges, thus suppressing the ordering of S_8 molecules into solid crystals. In addition, the marginal oxidization layer around H_2-MoS_2 plays a considerable role in delocalizing the electric field at the edges upon charging. By quantitatively analyzing the size and number of sulfur droplets with charging time, it is illustrated that the liquid

sulfur formation on H_2-MoS_2 follows diffusion-control growth kinetics and droplet-merging growth models. The rapid coalescence of droplets can release the active H_2-MoS_2 surfaces for a further polysulfide redox reaction, resulting in high areal capacities.

In contrast, the systems using pristine MoS_2 substrates present solid sulfur propagation from the edge to the basal area, indicating much lower areal capacities under the same measurement conditions. To demonstrate the universality of this strategy, we further annealed other transition metal dichalcogenides (TMDs) under H_2, which delivers similar growth behaviors: solid sulfur crystals form on pristine TMDs, whereas only liquid sulfur generates on H_2-treated ones. The environmental stability of the liquid sulfur is also investigated by decreasing the charging temperature from 25 °C to -50 °C, where sulfur droplets are still clearly observed on H_2-MoS_2 with high areal capacities, suggesting their promise for extremely low-temperature energy storage applications. This work sheds light on the mechanistic of sulfur formation on transition metal dichalcogenide substrates, which will expedite the development of a broad range of metal-liquid sulfur battery chemistries.

RESULTS AND DISCUSSION

Electrochemical generation of sulfur on MoS_2 and H_2-MoS_2

Figure 1a presents a schematic illustration of the electrochemical setup to generate sulfur on MoS_2 substrates by charging the catholyte (a mixture of 0.25 M Li_2S_8 and 0.5 M LiTFSI in dimethoxyethane/ 1,3-dioxolane) with Li-ion from the Li metal counter electrode.[18] To exclude the thickness effect of MoS_2 on sulfur formation behaviors, thick MoS_2 flakes (50-150 nm) were prepared on a Si/SiO_2 substrate by mechanically exfoliating bulk MoS_2 crystals. The MoS_2 was then annealed in an H_2 atmosphere at 600 °C for 10 h before being connected with titanium (Ti) micro-current collectors and sealed with a glass slide cover. It is noted that H_2 annealing effectively

tunes the chemical structures and electronic properties of MoS_2.[19] Ti is selected to build the MoS_2 cathode because it is inactive to the sulfur formation, even charging up to 4.0 V.[17] Before applying an external voltage of 2.8 V to drive the electrochemical reactions, the open circuit potential of the micro-device was measured to be ~2.4 V (Figure S1), consistent with that in actual batteries.

The electrochemical formation of sulfur on MoS_2 and H_2-MoS_2 was first observed by the *in-situ* optical microscopy as shown in the time-sequential images in Figures 1b and 1c and Movies S1 and S2 (Supporting Information). On pristine MoS_2 (Figure 1b and Movie S1), it is observed that liquid sulfur droplets (in light contrast) nucleated and grew at the beginning and then transferred to the solid phase (in dark contrast, at 120 seconds) once in contact with the solid sulfur generated on edges. The insulating solid sulfur continued to expand and occupy the entire basal planes by the end of charging. These observations agree well with the previous studies,[20] indicating the reliability of the electrochemical device in this work. In contrast, the delithiation of polysulfides on H_2-MoS_2, as depicted in Movie S2 and Figure 1c presents no contrast transition from light to dark of the sulfur product over the whole charging process, implying only liquid sulfur formation. The growth of the sulfur on H_2-MoS_2 is associated with the coalescence of adjacent droplets (as shown by the arrow in Figure 1c), releasing the conductive basal plane for additional liquid sulfur formation. This phenomenon will benefit high areal capacities in actual Li-S batteries. The merged sulfur droplet on H_2-MoS_2 can be up to 67.5 μm, approximately five times larger than the 13.6 μm of solid sulfur crystals formed on MoS_2. Such a difference further suggests the preservation of liquid sulfur on H_2-MoS_2 due to the reshaping capability of liquid sulfur. In addition, the linear scanning voltammetry (LSV) result demonstrates that the Li_2S_8 conversion to sulfur on the H_2-MoS_2 substrate possesses a smaller overpotential (Figure S2) than that of the MoS_2 substrate, which illustrates the higher redox kinetics on H_2-MoS_2.

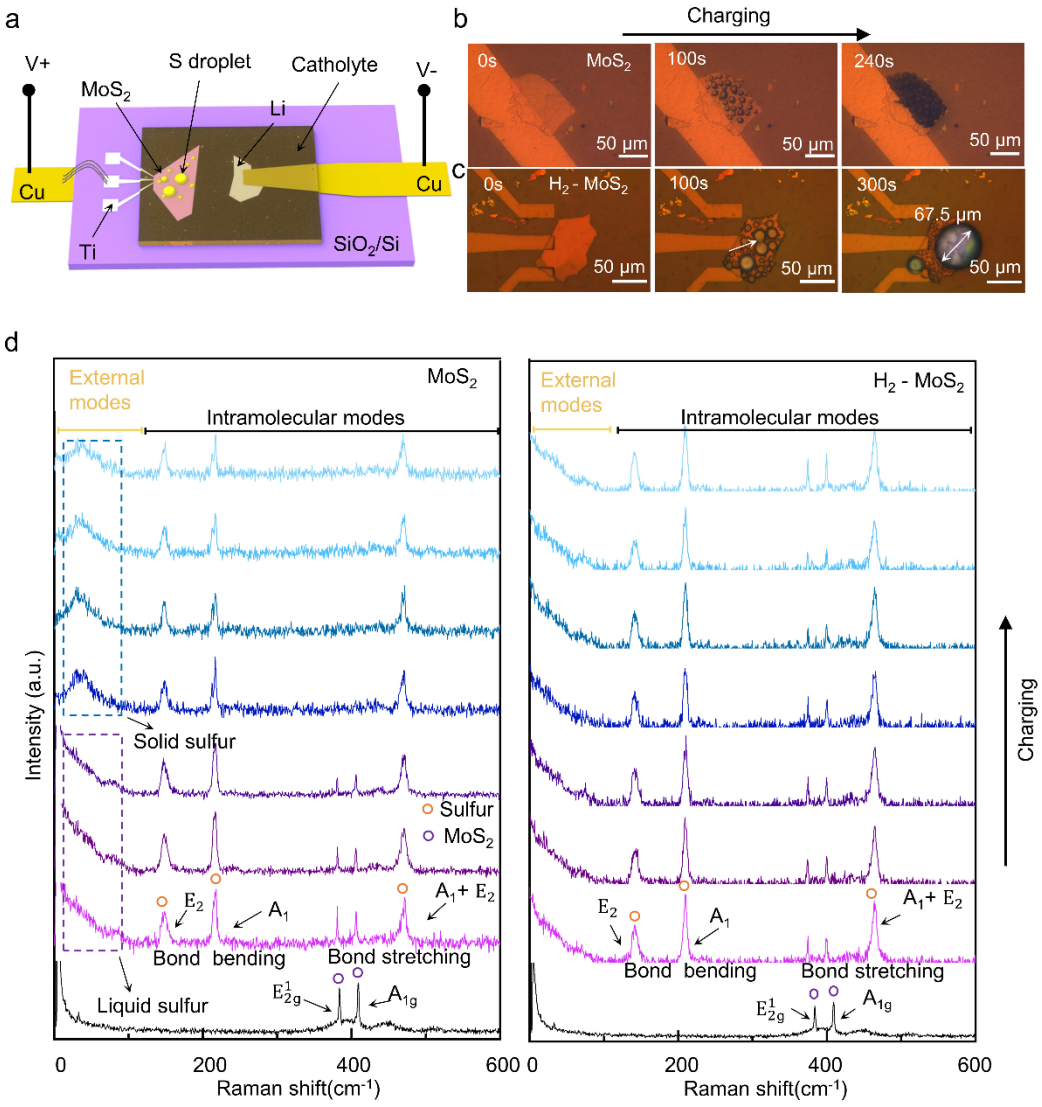

Figure 1. Sulfur generation on MoS_2 and H_2-MoS_2. a. The schematic of the optical cell. Optical images of sulfur droplets generation with time on **b** pristine MoS_2, and **c** H_2-MoS_2 at 2.8V. **d.** Evolution of Raman spectra on the pristine MoS_2 (left) and the H_2-MoS_2 (right) during charging.

The *in-situ* Raman spectroscopy study was also conducted to confirm the chemical structures of sulfur formed on MoS_2 and H_2-MoS_2, as shown in Figure 1d. Notable is that the micro-Raman spectrometer possesses sufficient spatial resolution (500 nm) to focus on individual sulfur droplets or particles. For the Raman signatures of sulfur, the internal vibration peaks at 153 cm^{-1}, 220 cm^{-}

[1], and 473 cm^{-1}, corresponding to the asymmetric vibration, symmetric vibration, and stretching of S-S bonds in the S_8 ring, are independent of the liquid or solid phase of sulfur (Figure 1d). In the low-frequency region (<100 cm^{-1}), solid β-sulfur and liquid sulfur droplets can be easily distinguished by the widened doublet peaks at 33 cm^{-1} and 42 cm^{-1} for the former and the smooth and Rayleigh wing-like slop for the latter, respectively.[21] It is worth noting that liquid sulfur cannot block the substrate signal. Thus, the feature peaks of MoS_2 are still identified by the Raman spectra, whereas the Raman signal of MoS_2 is hardly detected for the coverage of solid sulfur. According to these fingerprint features, it is observed that over the whole charging process, only liquid sulfur was detected on the surface of H_2-MoS_2, which is different from the liquid-solid phase transition of the sulfur product on MoS_2 upon charging. We also conducted *in-situ* optical and Raman characterization of the H_2-MoS_2-based electrochemical cells under different overpotentials of 2.6 V, 3.0 V, 3.2 V, and 3.5 V (see details in Figure S3-S5). All the samples present solitary formation of liquid sulfur during the whole charging process, suggesting the overpotential independent nature of the liquid sulfur generation on H_2-MoS_2.

In order to demonstrate the universality of the liquid sulfur generation and preservation on H_2-annealed transition metal dichalcogenides (TMDs), we also prepared other 2D materials before and after annealing in H_2, *i.e.*, WS_2, H_2-WS_2, $MoSe_2$, and H_2-$MoSe_2$ (See details in Supporting Information), for the *in-situ* optical and Raman characterization. We observed similar sulfur growth behaviors as mentioned above for the pristine and H_2-TMDs: only liquid sulfur droplets were generated on the H_2-WS_2 and H_2-$MoSe_2$, whereas the surface of pristine $MoSe_2$ and WS_2 are covered by solid sulfur crystals (Figure 2a, b, and Movie S3-S6) eventually. The sulfur phases on the different substrates were confirmed by Raman spectroscopy (Figure 2c). It is noteworthy that solid sulfur is directly growing from the edge and propagating to the basal plane of pristine WS_2,

whereas only liquid sulfur droplets can be formed on H_2-WS_2. The different solid sulfur growing behavior on WS_2, $MoSe_2$ and MoS_2 may be attributable to their dissimilar binding energies with sulfur species. For example, WS_2 was calculated to show a stronger affinity to LiPSs than MoS_2 and $MoSe_2$.[18] Together with the intensive electric field at the edges of semi-conductive WS_2, direct solid sulfur formation from the WS_2 edges was observed. All the above evidence demonstrates that liquid sulfur generation in an electrochemical system at room temperature is achievable on H_2-TMD substrates.

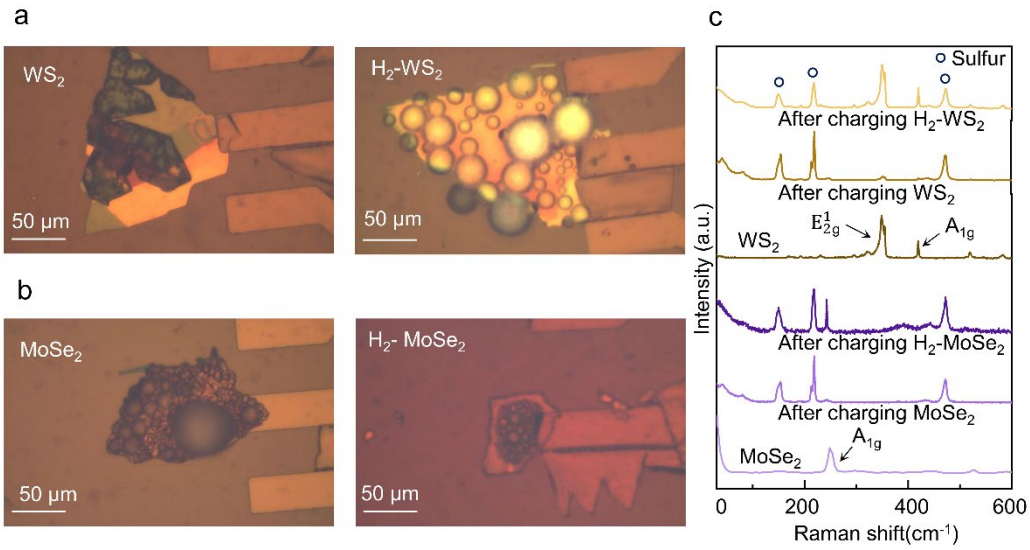

Figure 2. Sulfur generation on other pristine TMDs and H_2 treated TMDs. a. The optical images of solid sulfur and liquid sulfur formed on the WS_2 and H_2-WS_2 flakes, respectively. **b**. The optical images of solid sulfur and liquid sulfur formed on $MoSe_2$ and H_2-$MoSe_2$ flakes, respectively. **c**. The Raman spectra of $MoSe_2$, H_2-$MoSe_2$, WS_2, and H_2-WS_2 flakes before and after charging in the optical cell.

Sulfur growing dynamics on MoS_2 and H_2-MoS_2

Before explaining the distinct sulfur formation behaviors on MoS_2 and H_2-MoS_2, we investigate the liquid sulfur growing dynamics lacking in previous studies. The nucleation and growth kinetics

of sulfur droplets are studied by quantitatively analyzing the droplet size and number with charging time, as shown in Figure 3. Notably, the growth of the sulfur droplets on the substrate is accomplished by the coalescence of adjacent particles and the isotropic growth of individual particles (Figure S6). For the sulfur growing kinetics study, we selected droplets driven by the delithiation of polysulfides without coalescence occurring. Accordingly, we choose three droplets on H_2-MoS_2 (designated as 1#, 2# and 3# with dash circles in Figure 3e) and another three on the MoS_2 (designated as 1, 2 and 3 with dash circles in Figure 3a) as control. It is observed that the sizes of the droplet 1 and 2 on the basal plane of MoS_2 approached 10 μm at approximately 80 seconds (Figure 3b), whereas it only needs around 48 seconds for 1# and 3# to reach this size on H_2-MoS_2 (Figure 3f). Thus, the average sulfur growing rate on H_2-MoS_2 is more than 1.5 times faster than on MoS_2. The faster-growing kinetics can be attributable to the tailored electrical conductivity or/and binding energy between sulfur species and H_2-MoS_2.[22] H_2 annealing introduces sulfur deficiency on the basal plane, which improves the electrical conductivity of MoS_2 (Figure S7).[23, 24] A closer examination shows that the change of droplets size becomes slower with time increase, which is consistent with the diffusion-controlled reaction.[25] Further studies are needed to elucidate the origin of the distinct kinetic transition behavior of sulfur growth in a liquid electrochemical system.

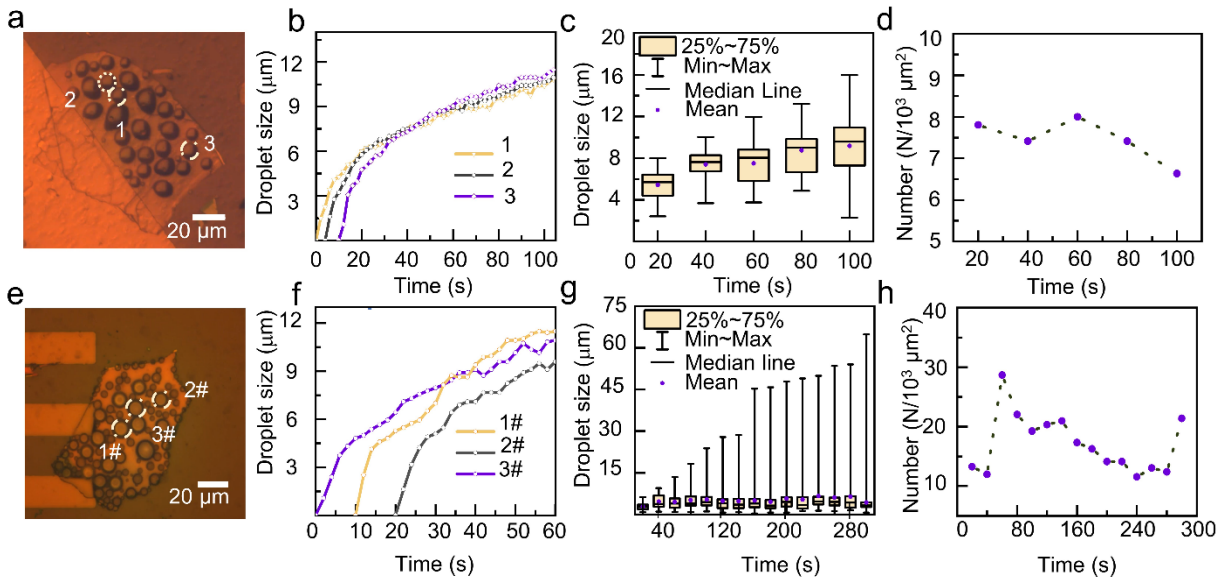

Figure 3. Liquid sulfur growth dynamics on MoS_2 and H_2-MoS_2. a. Optical image of the three chosen droplets marked as 1,2,3 on MoS_2. **b.** Growth behavior of the three droplets in **a. c**. Droplets size distribution during the charging process on MoS_2. **d**. Droplets number per 1000 μm^2 on MoS_2. **e**. Optical image of the three chosen droplets marked as 1#, 2#, 3# on H_2-MoS_2. **f**. Growth behavior of the three droplets in **e**. **g**. Droplets size distribution during the charging process on H_2-MoS_2. **h**. Droplets number per 1000 μm^2 of H_2-MoS_2.

We further examined the overall particle size distribution of the sulfur product as a function of time. The size distributions are plotted as bar graphs with the growth time in Figure 3g. At 20 seconds, the average droplet size on H_2-MoS_2 is 2.87 ± 1.25 μm, rendering a standard error of 15.9%. After 100 seconds, the standard deviation increases up to 3.83 μm, also the mean and median difference is 40.4%. The increasing disparity in size distribution with time suggests progressive nucleation of the sulfur droplets, which is described as the continuous formation of small nuclei during other particles growing on the substrate. Similar phenomena are also observed in the overall sulfur droplet size distribution on MoS_2 (Figure 3c). Therefore, it is evident that the

precipitation of sulfur on MoS_2 substrates follows the progressive nucleation model.[26] Interestingly, the number density of sulfur droplets on H_2-MoS_2 is continuously decreasing from 36.9×10^3 μm^{-2} at 80 seconds to 20.8×10^3 μm^{-2} at 280 seconds (Figure 3h). It means there is competition between the nucleation (increase the droplet number) and the coalescence (decrease the droplet number) process. The interfacial tension drives the coalescence of the contacted droplets to reduce the surface energy in the system. [27, 28] Apparently, the merging speed surpasses the nucleation speed of sulfur droplets between 80 and 280 seconds, which would free active surfaces on H_2-MoS_2 for excess sulfur deposition, leading to high areal capacities in practical batteries. In contrast, the number density of sulfur particles on MoS_2 exhibits slight fluctuation after solidification of sulfur droplets (Figure 3d), leading to complete coverage of the conductive host by insulating sulfur, rendering relatively low areal capacities (Figure S8). In brief, the progressive nucleation and droplet-merging growth models contribute to the aggressive growth of large sulfur droplets for high areal capacity Li-S batteries with H_2-MoS_2.

Mechanisms of entire liquid sulfur generation on H_2-MoS_2

To understand the different sulfur growing behaviors on MoS_2 and H_2-MoS_2, we first performed material characterization of these two substrates (Figure S9-S12). Optical microscopy (OM) and scanning electron microscopy (SEM) images reveal no apparent change in the overall morphology of MoS_2 after H_2 annealing treatment, except for some particles formed on the edge area of H_2-MoS_2 (Figures S9 and S10). Energy-dispersive spectroscopy (EDS) elemental maps indicate these particles as marginal MoO_x compounds. Then, to identify the chemical structures of H_2-MoS_2, we performed Raman, X-ray photoelectron spectroscopy (XPS), and X-ray diffraction (XRD). XPS spectra (Figure S11) show nonnegligible peaks referring to MoO_x.[29] Raman spectra (Figure S12) on the basal plane and edge area of H_2-MoS_2 are significantly different, with distinct features

referring to MoS_2 and MoO_2, respectively.[30] It means the edges of MoS_2 flakes are partially oxidized during the annealing process. The reason for the formation of MoO_x around the edges may be that the edges of MoS_2 are more easily reduced to low oxidation state Mo atoms and then oxidized in the air when the sample is removed from the furnace.[9, 31] To demonstrate the chemical structures of the edge areas, elemental mappings were conducted under SEM and scanning transmission electron microscopy (STEM). The energy-dispersive spectroscopy (EDS) mapping of the edge area under SEM displayed Mo: S: O atomic ratios of 1: 0.96: 2.23 (Figure S13a, b), demonstrating the severe oxidation at the edge area with discrete oxidized particles. A close look at the oxidized particles in STEM illustrates atomic ratios of approximate 1:1:1 for Mo: S: O (Figure S13 c-e), suggesting a mixture compound of MoS_2 and MoO_2, in agreement with the Raman result in Figure S12. Moreover, the integrated differential phase contrast (iDPC) STEM images show a possible hexagonal structure and detectable amounts of oxygen vacancies for the oxidized edge materials (Figure S14). Another interesting message derived from the Mo 3d XPS spectra of the MoS_2 and H_2-MoS_2 is the appearance of additional peaks at 232/229 eV, corresponding to sulfur-vacancy rich H_2-MoS_2. [29, 32] XRD patterns (Figure S15) and high-resolution TEM (HRTEM) images (Figure S16) confirmed that the 2H MoS_2 phase was kept intact. Thus, it is concluded that the H_2 annealing treatment can induce sulfur vacancies on the basal plane and partial oxidation on the edge of MoS_2.

Because the non-uniform electric field distribution at the edges was the critical factor contributing to the solid sulfur formation on MoS_2, the electric field distribution on H_2-MoS_2 is of primary interest in understanding the liquid sulfur formation. Therefore, we simulated the electric field distributions on H_2-MoS_2 and MoS_2 flakes by applying constant voltages of 2.8, 3.0, 3.2, and 3.5 V (Figure 4a, b and Figure S17). Compared with the intense polarization at the edges of MoS_2,

there is a buffer region to passivate the electric field distribution at the edges for H_2-MoS_2. In addition, the relative permittivity of MoO_2, the main component in MoO_x, is lower than that of MoS_2[33, 34] but is closer to that of the electrolyte. Thus, the MoO_x compounds could provide the transition of electric field distribution, as shown in Figure 4b. The iDPC-STEM image in Figure S18 clearly illustrates the different electric fields in the oxidized edge areas and the intact basal plane of H_2-MoS_2, consistent with the simulation results under constant external potentials.

Furthermore, the relatively homogeneous electric field at the edge of H_2-MoS_2 can decrease the local sulfur supersaturation and electrowetting effect, thus suppressing the ordering of S_8 molecules into solid crystals on the edges. In contrast, strongly localized partial charges and enhanced electric field appear at the edge of MoS_2 upon applying constant potentials, consistent with the previous report.[18] The enhanced driving force promoted the droplet wetting on the edge, which lowered the energy barrier from liquid to a solid phase transition, thus facilitating the crystallization of sulfur on the edge. The weakened wettability of liquid sulfur on H_2-MoS_2 edges can be directly evidenced by comparing the contact angles of sulfur droplets on MoS_2 materials. During the charging process, some sulfur droplets grew along the edge of MoS_2 flakes (Figures 4c and d), allowing us to measure the contact angles from the top view directly. The contact angle between sulfur droplets and H_2-MoS_2 was around 113°, almost twice the 56° contact angle between a sulfur hemisphere and pristine MoS_2. This result clearly illustrates much stronger wettability between sulfur droplets and MoS_2 than that for H_2-MoS_2. Thus, the poor wettability between H_2-MoS_2 and liquid sulfur, as well as the uniformed electric field distribution, play critical roles in preserving the liquid sulfur on the edge of H_2-MoS_2.

It is noted that the contact angles between sulfur droplets and MoS_2 measured in this work are different from the hypothesized 180º in the previous work.[18] To demonstrate the soundness of the

results in this work, we (i) analyzed the droplet merging behaviors in this work by assuming a 180º contact angle between droplet and MoS_2, and (ii) calculated the volumes of sulfur droplets using the geometric models with measured contact angles in this work. As marked by white arrows in Figure S19a, several small droplets (around 5 μm in size) are in physical contact with a large droplet of 31 μm in size on MoS_2 at 100 seconds. They merged later, as shown in the inset of Figure S19a. If the contact angle between sulfur droplet and MoS_2 is close to 180°, above adjacent droplets with significantly different sizes will be either disconnected from each other or not displaceable simultaneously (Figure S19b), which disagrees with the experimental observation. If the contact angle is less than 90°, such as 56º measured in this work, the equivalent between the experimental result and the model becomes reasonable and plausible.

Further, we calculated the volumes of two droplets before and after merging using a spherical cap model with the 56º contact angle (see details in Figure S19c, d). It shows that the volume of the merged droplet is almost equal to the sum of volumes of two-parent droplets. Furthermore, it is noted that the merging process only takes 0.1 seconds. Thus the growth of the droplets from polysulfide oxidation can be negligible. These results also suggest that the contact angle should not change significantly during coalescence. Based on this finding, we also calculated the total volumes of sulfur droplets on H_2-MoS_2 at different charging times, which display an accordant tendency with the areal capacities (Figure S20). Therefore, the contact angles measured for sulfur droplets and MoS_2 materials in this work are plausible and capable of predicting the wettability effect and furthering the solid sulfur growth behaviors.

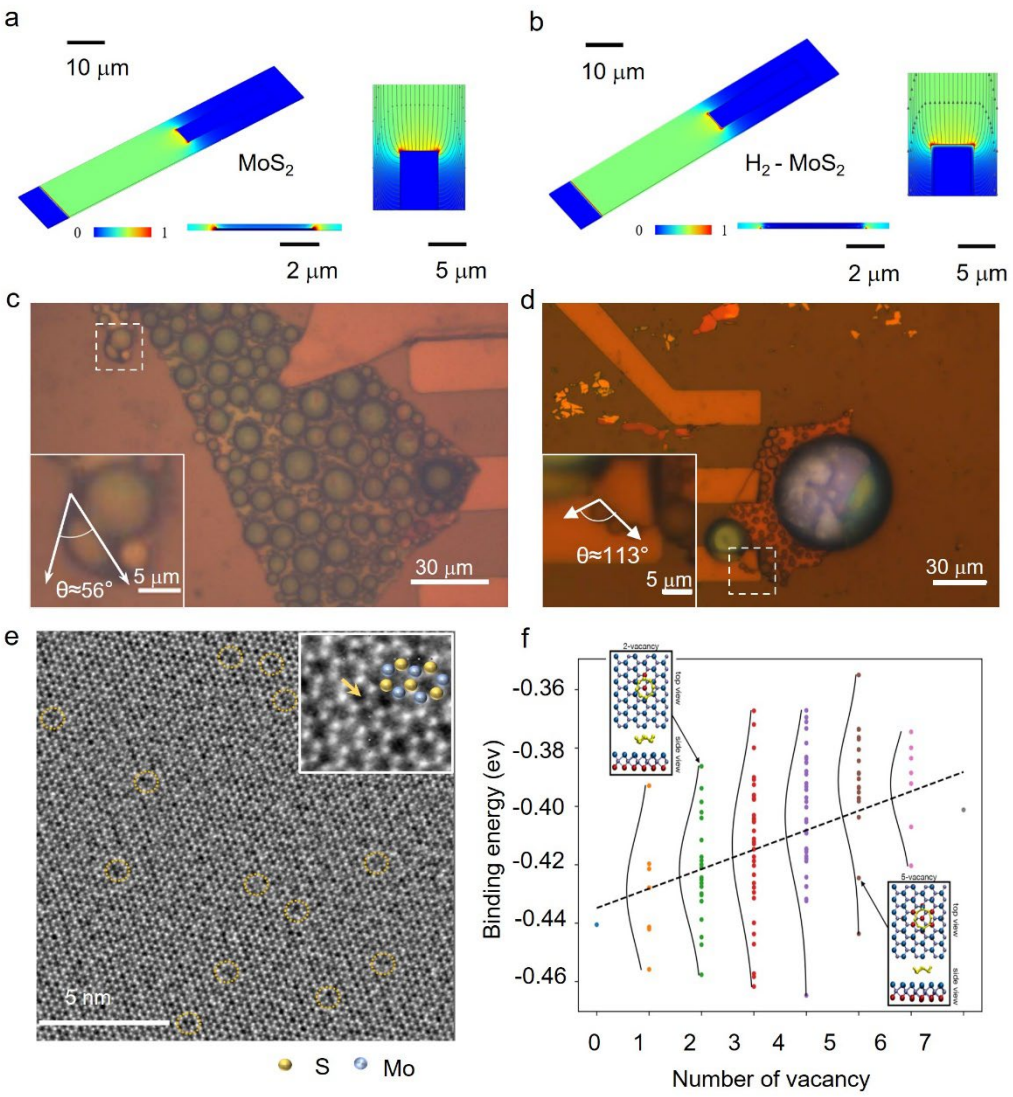

Figure 4. **The mechanism of liquid sulfur generation on H_2-MoS_2.** Electric field distribution on **a** MoS_2 and **b** H_2- MoS_2 at 2.8V. The optical images of liquid sulfur formed on **c** MoS_2 and **d** H_2-MoS_2 flakes. Insets are the contact angle between the sulfur droplet and the MoS_2 (or H_2-MoS_2) edge. **e**. iDPC-STEM image of H_2-MoS_2. Sulfur vacancies are highlighted by bash circles and an arrow (in the inset). **f**. The binding energy between the S_8 and MoS_2 as a function of sulfur vacancies.

The sulfur deficiency on the basal plane of H_2-MoS_2 is verified by the iDPC-STEM image, as shown in Figure 4e. To further probe the fundamentals of distinct sulfur growing behaviors on pristine MoS_2 and H_2-MoS_2, we also performed density functional theory (DFT) calculations. We evaluated the binding energy between the S_8 molecule and the surface of MoS_2 at various sulfur vacancy content. We selected 7 sulfur atoms of the upper layer of MoS_2 as being directly under the S_8 molecule. For a given number of sulfur vacancies (from 2 to 6), their precise location dramatically affects the binding energy (*e.g.*, 2 vacancies adjacent versus 2 vacancies away from each other). There are C_k^n combinations corresponding to k vacancies (k = 1 to 7) out of n = 7 sites giving a total of 128 structures and binding energies. Therefore, we developed an automatic procedure to compute all the 128 binding energies. It is clearly illustrated in Figure 4f that, on average, the magnitude of the binding energy between S_8 and H_2-MoS_2 decreases when the vacancies number increases. The weaker binding likely leads to the stabilization of liquid sulfur droplets.[18] The binding energies between S_8 and $MoSe_2$ with diselenide deficiency also have a similar change tendency, as shown in Figure S21, thus explaining the exclusive liquid sulfur formation on H_2-TMDs (Figure 2).

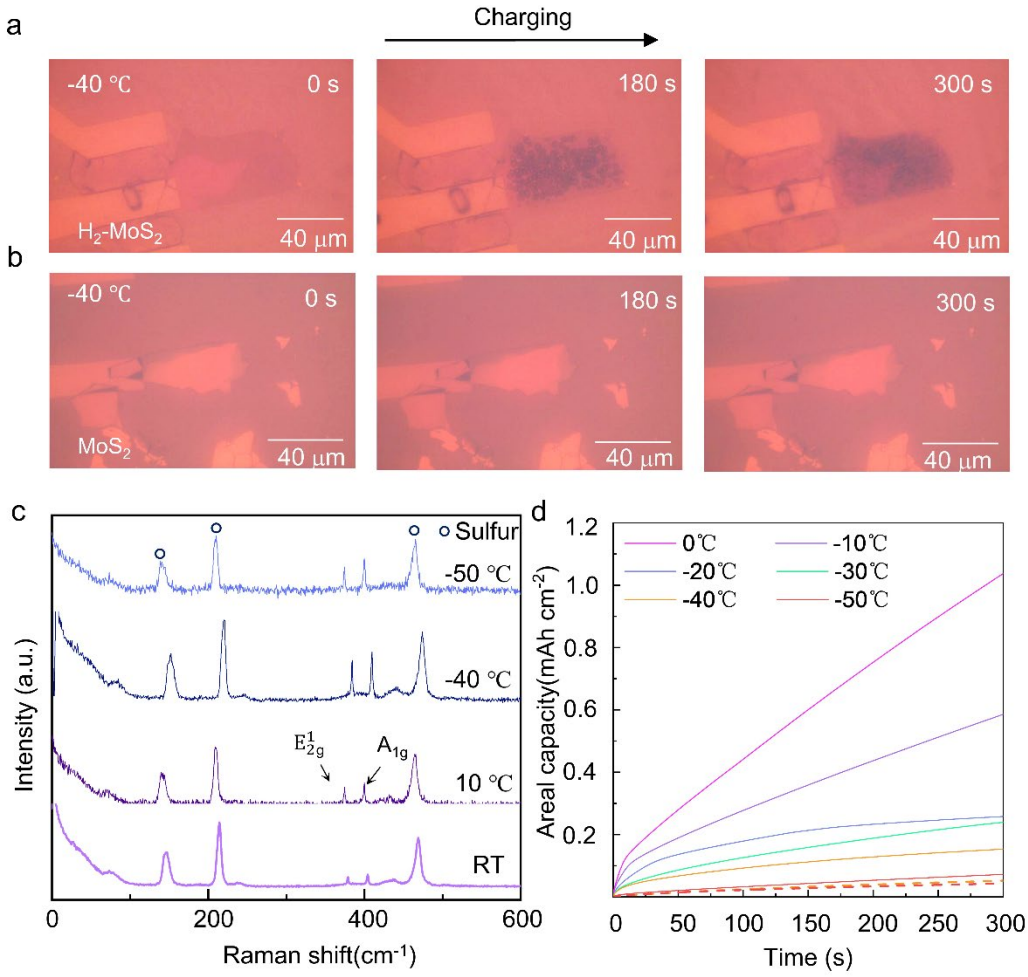

Figure 5. Low-temperature performance of the optical cell. In situ optical microscopy images of liquid sulfur generated on **a** H_2-MoS_2 and **b** MoS_2 at -40 °C. **c**. Raman spectra of liquid sulfur generation on H_2-MoS_2 at different temperatures. **d**. The areal capacities when charging the H_2-MoS_2-based optical cells at temperatures ranging from 0 to -50 °C (solid line) and MoS_2-based optical cells at temperatures -40 °C and -50 °C (dash line).

Furthermore, we found that the binding energy between the lithium polysulfide Li_2S_8 and the substrate increases with sulfur vacancies (Figure S22). It suggests that the defective substrate has more absorption efficiency to lithium polysulfide than pristine MoS_2,[11] which is beneficial to

polysulfide entrapment on H_2-MoS_2. The efficient absorption of polysulfide could correlate with higher kinetics of the electrocatalytic conversion of polysulfide.[33] The theoretical analysis demonstrates that the H_2-MoS_2 favors both the liquid sulfur preservation and the superior reaction kinetics, in total agreement with the above experimental observations.

Electrochemical performance of Li-liquid S cells working under low temperatures

Finally, to assess the electrochemical performance of the Li-liquid sulfur system, we tested the micro-Li-S cells with H_2-MoS_2 as working electrodes at decreasing temperatures ranging from room temperature (25 ℃) to -50 °C. We chose -50 °C as the lowest testing temperature because the dimethoxyethane solvent in the electrolyte can freeze below -58 °C.[34] Commercial batteries' capacity retention and rate performance deteriorate severely below 0 °C, and they can hardly work at -20 °C.[34, 35] Li-S batteries have the potential to be applied to a low-temperature condition not only for their high specific capacity but also for the low freezing point of electrolytes.[34] The micro-Li-S cells were located in a liquid nitrogen-controlled low-temperature device, as shown in Figure S23. When we applied an overpotential of 2.8 V to the electrochemical system, only liquid sulfur generation was observed on the H_2-MoS_2 at room temperature, 10 °C, -40 °C, and even -50 °C (Figure 5a, Figure S24 and Movie S7), which was confirmed by the Raman spectra with only Rayleigh wing features between 10 and 100 cm^{-1} (Figure 5c). The supercooling sulfur at -50 ℃, which is much lower than the melting temperature of 155℃, warrants further discussion. No solid sulfur formation implies the disordered nature of the sulfur molecular in the long range, which may be driven by the thermodynamic variations between liquid Li_2S_8 and S_8 under moderate electrochemical potentials. The low temperature (*i.e.*, -50 ℃) may induce glass transition of liquid sulfur, rendering decreased flowability.[16] The correlation among the working temperature, local potential, and the sulfur state requires more investigations in the future. In contrast, no reaction

occurred on the basal plane of MoS_2, as shown in Figure 5b and Figure S25 at -40℃ and -50℃. As the working temperature goes below 0 °C, it is notable that the optical observation was blurred by condensed moisture on the glass cover, but the flowable sulfur droplets are still detectable with light contrast color and merging phenomenon. Interestingly, at -40 °C and -50 °C, the size distributions of sulfur droplets formed on H_2-MoS_2 are more uniform than those generated at room temperature (Figure 1c). The difference should result from the significantly decreased merging rate (see Figure S26, the coalescence of two droplets takes 1 s, which is less than 0.1 s at room temperature) and the growing kinetics of individual droplets at extremely low temperatures. [16] The sluggish kinetics at the low temperature can be amenable by selecting temperature-insensitive ionic liquid electrolytes in future studies.[36]

Figure 5d presents the areal capacity profiles with charging time at 2.8 V when the working temperature decreases from 0 °C to -50 °C on MoS_2 and H_2-MoS_2 within 5 minutes. It shows the cells can retain liquid sulfur and deliver appreciable areal capacities of 1.037, 0.153, and 0.07 mAh cm^{-2} at 0, -40, and -50 °C on H_2-MoS_2. In contrast, the MoS_2 cell only attributes 0.052 mAh cm^{-2} and 0.043 mAh cm^{-2} at -40, and -50 °C (dash line), which is lower than the H_2-MoS_2 cell. The liquid sulfur sustaining at ultra-low temperature may be attributed to higher reaction kinetics for the Li_2S_8 reduced to liquid sulfur than solid sulfur. However, the coalescence process becomes difficult for the large viscosity of liquid sulfur at low temperatures,[16] and the droplet growth mainly relies on independent growth. The general testing temperature for low-temperature LSBs is -20 °C, regarded as the 'deadline' for a battery test.[34, 35] To estimate the standing of the electrochemical performance current Li-liquid sulfur system among the reported low-temperature LSBs, we calculated the areal capacity for the whole charging process. It is found that the capacity has the potential to arrive at 1.22 mAh cm^{-2} at -40 °C. The Li-liquid-sulfur system would exclude the need

for battery warming in previous LIB systems [35] due to their universal operating capability at ultra-low temperatures.

CONCLUSIONS

In summary, we have demonstrated stable liquid-sulfur generation on H_2-annealed MoS_2 substrates during the delithiation of polysulfides. The liquid-sulfur formation is progressive, rapid merging and growing, leading to exceptionally large sulfur droplets and high areal capacities. The phenomenon has never been observed in conventional Li-solid-sulfur electrochemical systems. The intriguing liquid sulfur chemistry originates from the partially oxidized layer around the edge of MoS_2 and sulfur vacancies on the basal plane of MoS_2, which effectively tune the electric field distribution and the binding energies to sulfur molecules with H_2-MoS_2 substrates. We have also demonstrated competitive areal capacities and ultra-stable liquid sulfur phases in the H_2-MoS_2-based electrochemical system, decreasing the operating temperature to -50 °C, which has been very difficult for commercial Li-ion batteries and Li-solid sulfur batteries to survive. We believe that the concept of stable liquid sulfur formation on hydrogen-treated TMDs will spur extensive research interest in liquid sulfur-based flow batteries, fast-charging batteries, and low-temperature energy storage technologies.

METHODS/EXPERIMENTAL

Optical cell fabrication

The scotch tape method was used to prepare MoS_2, $MoSe_2$, and WS_2 flakes on 300-nm-thick SiO_2/Si substrate. Then the samples were placed in a 5% H_2/ Ar atmosphere at 600 ℃ for 10 h to prepare H_2-treated TMD materials. Photolithography (Suss ma6 mask aligner) and electron beam deposition of titanium were used to prepare the electrodes (50 - 70 nm). The prepared device and the copper foil were set on the glass slide, and aluminum bonding wires were applied to create

electric interconnections between the titanium electrode and copper foil. A suitable-sized glass plate was placed to cover the two electrodes. One of the electrodes was the titanium on the TMD flakes as the cathode. Another was lithium metal pressing on the copper foil as the anode (only have copper now), and then the cover glass was fixed by Kapton tape (only on the cathode side). The following steps to fabricate the device would be finished in the argon-filled glove box. Lithium metal was pressed on the copper foil, and the Kapton tape was used to fix the cover glass on the anode side. About 1.75 M sulfur, 0.25 M Li_2S, 0.5 M LiTFSI, and 0.1 M $LiNO_3$ were dissolving in DOL: DME 1:1 (v/v) solution and mixed at 60 °C for 24 h to prepare 0.25 M Li_2S_8 catholyte. The catholyte was added into the cell, relying on the capillary effect, and the unsealed sides were sealed by vacuum grease (Dow Corning) directly.

***In situ* optical microscopy**

The cell was potentiostat charged and galvanostatic discharged using an electrochemical workstation (CHI 760e). Meanwhile, optical microscopy (Leica Dm 2700M) with a dry-immersion objective (N PLAN L 50x/0,50) was applied to record the videos and images. The videos were taken by 1 frame/second at room temperature with an image resolution of 4.99 megapixels unless otherwise mentioned.

In situ Raman and low-temperature testing

Confocal Raman microscopy (alpha300 R, WITec Inc) was applied to characterize the sulfur using 532 nm excitation, and record the video 1 frame/second with an image resolution of 1.3 megapixels unless otherwise mentioned by the 50× microscope objective. The accumulation time was 10 seconds to get the Raman signal.

The cell was put on a temperature-controlled stage (DSC600) and measured by confocal Raman microscopy. A T96 controller, an LNP95 liquid nitrogen pump, and the linksys32 software

controlled the stage temperature. Before cooling down, dry nitrogen was used to purge all air out of the chamber to avoid the influence of water in the air. After starting the low-temperature testing, the liquid nitrogen pump kept working until the experiment finished.

Linear sweep voltammetry measurement

The preparation of cells is the same as for optical cells. The cell was tested from open circuit voltage to 2.8V with a scanning rate of 0.3 mV s^{-1}.

Material characterization

A Scanning Electron Microscope (Tescan VEGA3) with X-ray analysis of elements was used to observe the morphology and analyze composition. Field Emission Electron Microscope (STEM, JEM-2100f) was used to identify the structure of the sample. High-angle annular dark-field scanning TEM was used to acquire the atomic arrangement and analyze the materials' composition and electric field. Helios 5CX dual-beam focused ion beam (FIB) system was used to prepare the cross-sectional STEM samples. XPS (Thermo Scientific Nexsa) was used to measure the electronic state of the element. XRD (Rigaku SmartLab) was used to identify the phase.

DFT calculations

DFT calculations have been performed with VASP[1, 2] with the Perdew, Burke, and Ernzerhof functional [3]. Based on the rectangular unit cell, simulation cells consist of a single layer of MoS_2 replicated 3×6 (with various S vacancies). We used a 35 Å supercell to ensure no interactions between atoms and periodic images in the direction perpendicular to the surface. To adequately describe vdW interactions between MoS_2 surface and S8, we used the DFT-D2 correction proposed by Grimme and coworkers [4]. Due to a large number of calculations, we performed only Gamma point calculations and used a 400 eV kinetic energy cutoff. All molecular structures were

optimized until energy and forces reached a minimum of 10^{-6} eV and 5×10^{-2} eV/Å, respectively. Binding energies were calculated as:

$E_b = E_{S8@MoSx} - E_{S8} - E_{MoSx}$

with E_{S8}, E_{MoSx} and $E_{S8@MoSx}$, the energy of the S_8 molecule, defective MoS_2 and S_8 adsorbed on top of MoS_x, respectively.

Electric field simulation

Electric field simulations were conducted by the AC/DC physics module of COMSOL Multiphysics. The geometry of the MoS_2 flack was 20 μm × 5 μm × 100 nm. 400nm wide MoO_2 surrounded the MoS_2 flack, so the dimension of H_2 treated MoS_2 was 20.8 μm × 5.8 μm × 100 nm. The MoS_2 or H_2 treated MoS_2 was placed between two electrodes, and the distance between the two electrodes was 50 μm. The ether-based lithium-ion battery electrolyte (as system environment), MoS_2, MoO_2 are 7, 16[5], and 9.5[6], respectively. The Li anode was grounded, and the Ti cathode was applied constant volt of 3.0 V, 3.2V, and 3.5V.

ASSOCIATED CONTENT

Supporting Information

The Supporting Information is available free of charge at

Additional LSV curves, *in situ* optical microscopy photos and videos, Raman spectra, capacity measurements, SEM images, HAADF-STEM-EDS images, and DFT calculations results.

Author contributions

S.P.L. and Z.L.X. conceived the idea; S.P.L. supervised the project; F.S. and Z.L.X. designed and conducted the experiments; C.C., Y.L., L.Z., and L.Z. support the characterization of materials and devices fabrication; N.O. performed DFT calculations; S.C. conducted TEM and HAADF-

STEM-EDS characterization; F.S., Z.L.X. and S.P.L. wrote the manuscript; all the authors commented on the manuscript.

ACKNOWLEDGMENTS

The work described in this paper was supported by grants from the Research Grant Council of Hong Kong Special Administrative Region, China (Project No. PolyU15303219, PolyU25216121), the National Natural Science Foundation of China-Young scholar (Project No. 52102310), the Research Committee of The Hong Kong Polytechnic University under project codes of 1-ZVGH, 1-BE3M, A-PB1M, 1-BBXK, and G-UAMV. In addition, we are grateful for Ki Hei Wong providing the low-temperature testing devices and Lukas Rogée for TEM assistance.

Notes

The authors declare no competing financial interest.

REFERENCES

(1) Xu, Z.-L.; Kim, J.-K.; Kang, K. Carbon Nanomaterials for Advanced Lithium Sulfur Batteries. *Nano Today* **2018**, *19*, 84-107.

(2) Seh, Z. W.; Sun, Y.; Zhang, Q.; Cui, Y. Designing High-Energy Lithium-Sulfur Batteries. *Chem. Soc. Rev.* **2016**, *45*, 5605-5634.

(3) Hu, Y.; Chen, W.; Lei, T.; Jiao, Y.; Huang, J.; Hu, A.; Gong, C.; Yan, C.; Wang, X.; Xiong, J. Strategies Toward High-loading Lithium-Sulfur Battery. *Adv. Energy Mater.* **2020**, *10*, 2000082.

(4) Li, T.; Bai, X.; Gulzar, U.; Bai, Y. J.; Capiglia, C.; Deng, W.; Zhou, X.; Liu, Z.; Feng, Z.; Proietti Zaccaria, R. A Comprehensive Understanding of Lithium–Sulfur Battery Technology. *Adv. Funct. Mater.* **2019**, *29*, 1901730.

(5) Zhang, M.; Chen, W.; Xue, L.; Jiao, Y.; Lei, T.; Chu, J.; Huang, J.; Gong, C.; Yan, C.; Yan, Y.; Hu, Y.; Wang, X.; Xiong, J. Adsorption-Catalysis Design in the Lithium-Sulfur Battery. *Adv. Energy Mater.* **2019**, *10*, 1903008.

(6) Yang, X.; Li, X.; Adair, K.; Zhang, H.; Sun, X. Structural Design of Lithium–Sulfur Batteries: From Fundamental Research to Practical Application. *Electrochemical Energy Reviews* **2018**, *1*, 239-293.

(7) Wang, X.; Gao, T.; Fan, X.; Han, F.; Wu, Y.; Zhang, Z.; Li, J.; Wang, C. Tailoring Surface Acidity of Metal Oxide for Better Polysulfide Entrapment in Li-S Batteries. *Adv. Funct. Mater.* **2016**, *26*, 7164-7169.

(8) Jiao, L.; Zhang, C.; Geng, C.; Wu, S.; Li, H.; Lv, W.; Tao, Y.; Chen, Z.; Zhou, G.; Li, J.; Ling, G.; Wan, Y.; Yang, Q. H. Capture and Catalytic Conversion of Polysulfides by In Situ Built TiO_2-MXene Heterostructures for Lithium-Sulfur Batteries. *Adv. Energy Mater.* **2019**, *9*, 1900219.

(9) Xu, Z.-L.; Kim, S. J.; Chang, D.; Park, K.-Y.; Dae, K. S.; Dao, K. P.; Yuk, J. M.; Kang, K. Visualization of Regulated Nucleation and Growth of Lithium Sulfides for High Energy Lithium Sulfur Batteries. *Energy Environ. Sci.* **2019**, *12*, 3144-3155.

(10) Zhang, L.; Qian, T.; Zhu, X.; Hu, Z.; Wang, M.; Zhang, L.; Jiang, T.; Tian, J. H.; Yan, C. In Situ Optical Spectroscopy Characterization for Optimal Design of Lithium-sulfur Batteries. *Chem. Soc. Rev.* **2019**, *48*, 5432-5453.

(11) Xu, Z.-L.; Onofrio, N.; Wang, J. Boosting the Anchoring and Catalytic Capability of MoS_2 for High-loading Lithium Sulfur Batteries. *J. Mater. Chem. A* **2020**, *8*, 17646-17656.

(12) Waluś, S.; Barchasz, C.; Bouchet, R.; Leprêtre, J.-C.; Colin, J.-F.; Martin, J.-F.; Elkaïm, E.; Baehtz, C.; Alloin, F. Lithium/Sulfur Batteries Upon Cycling: Structural Modifications and

Species Quantification by In Situ and Operando X-Ray Diffraction Spectroscopy. *Adv. Energy Mater.* **2015**, *5*, 1500165.

(13) Yang, Z.; Zhu, Z.; Ma, J.; Xiao, D.; Kui, X.; Yao, Y.; Yu, R.; Wei, X.; Gu, L.; Hu, Y.-S.; Li, H.; Zhang, X. Phase Separation of Li_2S/S at Nanoscale during Electrochemical Lithiation of the Solid-State Lithium–Sulfur Battery Using In Situ TEM. *Adv. Energy Mater.* **2016**, *6*, 1600806.

(14) Wang, Z.; Tang, Y.; Zhang, L.; Li, M.; Shan, Z.; Huang, J. In Situ TEM Observations of Discharging/ Charging of Solid-State Lithium-Sulfur Batteries at High Temperatures. *Small* **2020**, *16*, e2001899.

(15) Gorlin, Y.; Patel, M. U. M.; Freiberg, A.; He, Q.; Piana, M.; Tromp, M.; Gasteiger, H. A. Understanding the Charging Mechanism of Lithium-sulfur Batteries Using Spatially Resolved Operando X-ray Absorption Spectroscopy. *J. Electrochem. Soc.* **2016**, *163*, A930-A939.

(16) Liu, N.; Zhou, G.; Yang, A.; Yu, X.; Shi, F.; Sun, J.; Zhang, J.; Liu, B.; Wu, C. L.; Tao, X.; Sun, Y.; Cui, Y.; Chu, S. Direct Electrochemical Generation of Supercooled Sulfur Microdroplets Well Below Their Melting Temperature. *Proc. Natl. Acad. Sci. U.S.A.* **2019**, *116*, 765-770.

(17) Zhou, G.; Yang, A.; Wang, Y.; Gao, G.; Pei, A.; Yu, X.; Zhu, Y.; Zong, L.; Liu, B.; Xu, J.; Liu, N.; Zhang, J.; Li, Y.; Wang, L. W.; Hwang, H. Y.; Brongersma, M. L.; Chu, S.; Cui, Y. Electrotunable Liquid Sulfur Microdropletsopy. *Nat. Commun.* **2020**, *11*, 606.

(18) Yang, A.; Zhou, G.; Kong, X.; Vila, R. A.; Pei, A.; Wu, Y.; Yu, X.; Zheng, X.; Wu, C. L.; Liu, B.; Chen, H.; Xu, Y.; Chen, D.; Li, Y.; Fakra, S.; Hwang, H. Y.; Qin, J.; Chu, S.; Cui, Y. Electrochemical Generation of Liquid and Solid Sulfur on Two-dimensional Layered Materials with Distinct Areal Capacities. *Nat. Nanotechnol.* **2020**, *15*, 231-237.

(19) Ye, G.; Gong, Y.; Lin, J.; Li, B.; He, Y.; Pantelides, S. T.; Zhou, W.; Vajtai, R.; Ajayan, P. M. Defects Engineered Monolayer MoS_2 for Improved Hydrogen Evolution Reaction. *Nano Lett.* **2016**, *16*, 1097-1103.

(20) Xiang, Y.; Zheng, G.; Liang, Z.; Jin, Y.; Liu, X.; Chen, S.; Zhou, K.; Zhu, J.; Lin, M.; He, H.; Wan, J.; Yu, S.; Zhong, G.; Fu, R.; Li, Y.; Yang, Y. Visualizing the Growth Process of Sodium Microstructures in Sodium Batteries by *In-situ* ^{23}Na MRI and NMR Spectroscopy. *Nat. Nanotechnol.* **2020**, *15*, 883-890.

(21) Nims, C.; Cron, B.; Wetherington, M.; Macalady, J.; Cosmidis, J. Low Frequency Raman Spectroscopy for Micron-Scale and in Vivo Characterization of Elemental Sulfur in Microbial Sampleses. *Sci. Rep.* **2019**, *9*, 7971.

(22) Wang, H.-E.; Li, X.; Qin, N.; Zhao, X.; Cheng, H.; Cao, G.; Zhang, W. Sulfur-Deficient MoS_2 Grown Inside Hollow Mesoporous Carbon as A Functional Polysulfide Mediator. *J. Mater. Chem. A* **2019**, *7*, 12068-12074.

(23) Liu, B.; Ma, C.; Liu, D.; Yan, S. Sulfur-Vacancy Defective MoS_2 as a Promising Electrocatalyst for Nitrogen Reduction Reaction under Mild Conditions. *ChemElectroChem* **2021**, *8*, 3030-3039.

(24) Wang, H.; Xu, X.; Neville, A. Facile Synthesis of Vacancy-Induced 2H-MoS_2 Nanosheets and Defect Investigation for Supercapacitor Application. *RSC Adv.* **2021**, *11*, 26273-26283.

(25) Goodrich, F. C. On Diffusion-Controlled Particle Growth the Moving Boundary Probleme. *J. Phys. Chem.* **1966**, *70*, 3660-3665.

(26) Huang, W.; Li, J.; Xu, Y. Nucleation/Growth Mechanisms and Morphological Evolution of Porous MnO_2 Coating Deposited on Graphite for Supercapacitor. *Mater.* **2017**, *10*, 1205.

(27) Dahiya, P.; Caggioni, M.; Spicer, P. T. Arrested Coalescence of Viscoelastic Droplets: Polydisperse Doublets. *Philos. Trans. R. Soc. A* **2016**, *374*, 20150132.

(28) Nam, Y.; Kim, H.; Shin, S. Energy and Hydrodynamic Analyses of Coalescence-Induced Jumping Droplets. *Appl. Phys. Lett.* **2013**, *103*, 3660-3665.

(29) Lin, H.; Yang, L.; Jiang, X.; Li, G.; Zhang, T.; Yao, Q.; Zheng, G. W.; Lee, J. Y. Electrocatalysis of Polysulfide Conversion by Sulfur-Deficient MoS_2 Nanoflakes for Lithium-Sulfur Batteries. *Energy Environ. Sci.* **2017**, *10*, 1476-1486.

(30) Kumari, L.; Ma, Y.-R.; Tsai, C.-C.; Lin, Y.-W.; Wu, S. Y.; Cheng, K.-W.; Liou, Y. X-ray Diffraction and Raman Scattering Studies on Large-Area Array and Nanobranched Structure of 1D MoO_2 Nanorodss. *Nanotechnology* **2007**, *18*, 115717.

(31) Kiriya, D.; Lobaccaro, P.; Nyein, H. Y.; Taheri, P.; Hettick, M.; Shiraki, H.; Sutter-Fella, C. M.; Zhao, P.; Gao, W.; Maboudian, R.; Ager, J. W.; Javey, A. General Thermal Texturization Process of MoS_2 for Efficient Electrocatalytic Hydrogen Evolution Reaction. *Nano Lett.* **2016**, *16*, 4047-4053.

(32) Wu, W.; Niu, C.; Wei, C.; Jia, Y.; Li, C.; Xu, Q. Activation of MoS_2 Basal Planes for Hydrogen Evolution by Zinc. *Angew. Chem. Int. Ed.* **2019**, *58*, 2029-2033.

(33) Jayan, R.; Islam, M. M. First-Principles Investigation of the Anchoring Behavior of Pristine and Defect-engineered Tungsten Disulfide for Lithium–Sulfur Batteries. *J. Phys. Chem. C* **2020**, *124*, 27323-27332.

(34) Gupta, A.; Manthiram, A. Designing Advanced Lithium-Based Batteries for Low-Temperature Conditions. *Adv. Energy Mater.* **2020**, *10*, 2001972.

(35) Deng, D. R.; Xue, F.; Bai, C. D.; Lei, J.; Yuan, R.; Zheng, M. S.; Dong, Q. F. Enhanced adsorptions to polysulfides on graphene-supported BN nanosheets with excellent Li-S battery performance in a wide temperature range. *ACS Nano* **2018**, *12*, 11120-11129.

(36) Holoubek, J.; Liu, H.; Wu, Z.; Yin, Y.; Xing, X.; Cai, G.; Yu, S.; Zhou, H.; Pascal, T. A.; Chen, Z.; Liu, P. Tailoring Electrolyte Solvation for Li Metal Batteries Cycled at Ultra-low Temperature. *Nat. Energy* **2021**, *6*, 303-313.